Materials Chemistry and Physics 367 (2026) 133024

Contents lists available at ScienceDirect

Materials Chemistry and Physics

journal homepage: www.elsevier.com/locate/matchemphys

Quantitative mapping of nanoparticle distribution in composite thin films by terahertz time-domain spectroscopy imaging

Can Koral [a,d,*], Michela Marsico [b], Angela De Bonis [b], Zahra Mazaheri [c,d], Gian Paolo Papari [c,d], Antonello Andreone [c,d]

[a] Department of Health Sciences, University of Basilicata, 85100, Potenza, Italy
[b] Department of Basic and Applied Sciences, University of Basilicata, 85100, Potenza, Italy
[c] Department of Physics "E. Pancini", University of Naples "Federico II", 80126, Napoli, Italy
[d] National Institute for Nuclear Physics, Naples Unit, 80126, Napoli, Italy

HIGHLIGHTS

- THz time-domain spectroscopy imaging enables non-contact thickness mapping of chitosan thin films.
- Effective medium inversion combined with THz imaging maps nanoparticle distribution in composite thin films.
- Local fill factor measurements confirm non-uniform Ag nanoparticle dispersion within the chitosan matrix.
- Quantitative error propagation validates that spatial variations exceed film-thickness-induced uncertainties.

ABSTRACT

Terahertz Time-Domain Spectroscopy (THz-TDS) imaging is employed for the non-invasive, quantitative mapping of nanoparticle distribution in composite thin films. Chitosan–silver nanoparticle films are used as a model system to validate the methodology. The complex refractive index of pure chitosan films is first determined and used to generate high-resolution thickness maps, confirming film homogeneity in its central region. Silver nanoparticle suspensions are independently characterized by THz-TDS, and their complex dielectric function was extracted using effective medium theory, supported by TEM-based size analysis. The dielectric functions of both matrix and inclusions are then used to invert the effective medium relation and retrieve local volumetric concentrations in the composite film. This approach enabled quantitative spatial mapping of the nanoparticle distributions in composite structures.

1. Introduction

Nanoparticle-based composite thin films are widely investigated for applications in energy storage, sensing, optoelectronics, and biomedical systems, where functional performance critically depends on the spatial distribution of the embedded nanofillers. Achieving homogeneous nanoparticle dispersion and controlled film thickness remains particularly challenging in solvent-cast systems, where evaporation-driven phenomena such as capillary flow, phase separation, and particle aggregation may induce local compositional gradients.

Reliable, non-destructive methods for quantitatively assessing thickness uniformity and nanoparticle distribution are therefore essential [1]. Terahertz Time Domain Spectroscopy (THz-TDS) provides direct access to the complex refractive index and absorption coefficient by measuring the electric field of broadband terahertz pulses in the time domain. Unlike conventional intensity-based spectroscopy, THz-TDS retrieves amplitude and phase information, enabling accurate dielectric characterization of thin films without destructive preparation. Its ability to penetrate non-metallic materials makes it particularly suitable for polymer-based composites.

In this work, chitosan–silver nanoparticle (Ag NP) films are used as a model system to demonstrate a quantitative THz-based mapping approach. Chitosan is a biopolymer highly valued for its low toxicity, inherent proton conductivity, and ability to form flexible, transparent films. Its versatility extends from biomedical applications, such as wound healing and heavy metal removal, to its emerging role as a polymer electrolyte in advanced energy technologies like fuel cells, batteries, supercapacitors, and sensors. To overcome the often-insufficient conductivity of pure chitosan for practical applications, its electrical properties can be significantly enhanced by incorporating conductive fillers, such as silver nanoparticles. These silver-doped chitosan nanocomposites exhibit enhanced relaxation dynamics and offer

* Corresponding author. Department of Health Sciences, University of Basilicata, 85100, Potenza, Italy
E-mail address: can.koral@unibas.it (C. Koral).

https://doi.org/10.1016/j.matchemphys.2026.133024
Received 25 May 2026; Received in revised form 25 July 2026; Accepted 13 August 2026
Available online 13 August 2026

considerable potential for terahertz technology applications, including high-speed communication, non-destructive imaging, sensing, and medical diagnostics [2–5].

Ag NP films were prepared using solvent casting, a method known for its simplicity but also for its susceptibility to thickness and compositional inhomogeneities. This process involves preparing a homogeneous solution of the polymer in a suitable solvent, typically an aqueous acetic acid solution and incorporating silver nanoparticles for composite formation [6–9]. The homogeneous solution is then poured onto a suitable container, and the solvent is subsequently removed through evaporation, leaving behind a solid polymer film.

In this regard, THz characterization is particularly promising for sensing and investigating material dynamics, especially for samples with limited volumes or when studying surface-related properties that differ from bulk counterparts.

To accurately interpret the macroscopic dielectric properties of such composite materials, effective medium theories are essential. The Landau-Looyenga mean field theory provides a suitable framework for modelling the effective permittivity of heterogeneous media [10,11]. This model is particularly appropriate for systems with dilute inclusions, such as Ag NP suspensions, and is used for composite systems like compacted powders, interpenetrating network structures, and heterogeneous polymer mixtures, provided the components do not exhibit strong metallic conductivity. A crucial aspect of the procedure is the independent characterization of the silver nanoparticles, particularly their size- and concentration-dependent dielectric function, which remains an area with limited literature, especially in the THz regime. Deviations from bulk silver behaviour are observed, underscoring the necessity of experimentally determining nanoparticle dielectric properties rather than relying on bulk tabulated values [12,13]. Terahertz Time Domain Spectroscopy has been widely used in the past as a "quasi-optical" tool for the measurement of nanostructural dispersion in polymeric based composites [14].

Moreover, when implemented in imaging mode, it allows spatially resolved mapping of dielectric properties. By combining spatial scanning with frequency-domain analysis, it becomes possible to correlate local variations in effective permittivity with nanoparticle concentration and to generate a map illustrating the particle number distribution across the specified area. This comprehensive investigation might be helpful in offering a better understanding of silver NP dispersion within the chitosan matrix and more in general of the spatial distribution of components within advanced nanocomposites, contributing to their optimized design and application [15–17].

Our study proceeds in three steps: (i) thickness and dielectric characterization of pure chitosan films, (ii) extraction of the complex dielectric function of isolated Ag nanoparticles from suspension measurements, and (iii) spatial inversion of the effective medium relation to map local nanoparticle fill factor within the composite film. This approach establishes a quantitative and non-destructive framework for evaluating nanoparticle dispersion in thin-film composites.

2. Materials and methods

2.1. Silver nanoparticle synthesis and chitosan solution preparation

Silver nanoparticles (Ag NPs) were synthesized by nanosecond laser ablation of a high-purity silver target (Goodfellow, 99.999%) directly in a 1 g/L chitosan solution. The chitosan solution was prepared by dissolving chitosan (100–300 kDa, 75% degree of deacetylation, Acros Organics) in 0.1% acetic acid (Sigma-Aldrich, 99.8%) under continuous stirring at 35 °C for 4 h until complete dissolution. Laser ablation was performed using a nanosecond Nd:YAG laser (Handy-YAG, Quanta System) operating at 532 nm, with a pulse duration of 7 ns, repetition rate of 10 Hz, and average power of 150 mW. The beam was focused vertically onto the silver target through a 50 mm focal length lens, producing a spot size of 0.8 mm and a fluence of 1.5 J/cm^2. Ablation was carried out for 45 min with the target immersed in 50 mL of solution, maintaining a liquid column height of 2 cm while continuously translating the target to minimize crater formation. The resulting Ag nanoparticle concentration (7 μg/cm^3) was determined gravimetrically from the mass difference of the silver target before and after ablation. For morphological analysis, the colloidal suspension was deposited onto holey carbon copper grids (Agar Scientific) and examined using a FEI TECNAI G2 F20 Transmission Electron Microscope (TEM) operating at 200 kV. It was reported that the method ensures the production of stable colloidal Ag NPs embedded within the polymeric solution, while preventing polymer degradation during the ablation process [18].

2.2. Film fabrication and morphological characterization

Free-standing films of pure chitosan and chitosan–Ag NP composites were fabricated by solvent casting. 20 ml of the respective solution were poured onto 25 × 25 mm^2 plates and dried at room temperature. This procedure yielded films with an average thickness of approximately 50 μm. For composite films, silver nanoparticles were incorporated at 0.8 wt% prior to casting.

TEM analysis was used to determine nanoparticle morphology and size distribution. The Ag NPs exhibit a predominantly spherical geometry with an aspect ratio of 1.2 and a mean diameter of 25 nm (Fig. 1(a and b)).

2.3. Thickness homogeneity assessment

Prior to THz-TDS imaging, thickness measurements were performed in 5 points on both pure and composite films, using a mechanical micrometer (JUWEL PLUS, ABC Tools) with a resolution of 10 μm, an accuracy of ±10 μm, and an anvil diameter of 6.4 mm. Since, the corresponding contact area roughly 40 times larger than the THz beam waist, they smooth over microscale fluid-flow variances. This specific scale mismatch highlights the value of our THz-TDS raster-scanning approach for tracking localized gradients.

Both film types exhibited similar thickness profiles (see Fig. 2(a) and (b)). The central region showed a thickness of approximately 50 μm, while values near the edges ranged between 45 and 70 μm. The composite film presented slightly lower thickness at two lateral borders; however, within experimental uncertainty, the overall profiles were comparable, confirming reproducibility of the casting process.

2.4. Terahertz Time Domain Spectroscopy setup

Terahertz Time Domain Spectroscopy was employed to thoroughly characterize pure chitosan films and colloidal silver nanoparticle suspensions, enabling the extraction of the respective refractive index and absorbance. TDS measurements were performed in transmission geometry using a commercial THz time-domain spectrometer (TERA K-15, Menlo Systems, Planegg, Germany) driven by a femtosecond laser. Two fiber coupled dipole photoconducting antennas (PCA) with linear polarization were employed for the emission and detection of the THz signal. The electric field was acquired over a total time-domain window of 120 ps. THz frequency domain analysis is conducted on the signals averaged over 500 waveforms, whereas imaging measurements are carried out using a single shot for each pixel. A pair of polymethylpentene (TPX) lenses (f = 50 mm, Tydex) for each emitter and detector arm was used to collimate and subsequently focus the radiation onto the samples, producing a focal beam waist of approximately 1 mm, which is also verified using the knife-edge technique. The experimental process involved separately acquiring time-domain signals through the sample at normal incidence and a free-space reference signal. To ensure transparency and demonstrate system performance, the raw time-domain waveforms are provided in a stacked panel layout in Fig. S1 of the Supporting Information.

After transferring the time-domain signals to the frequency domain

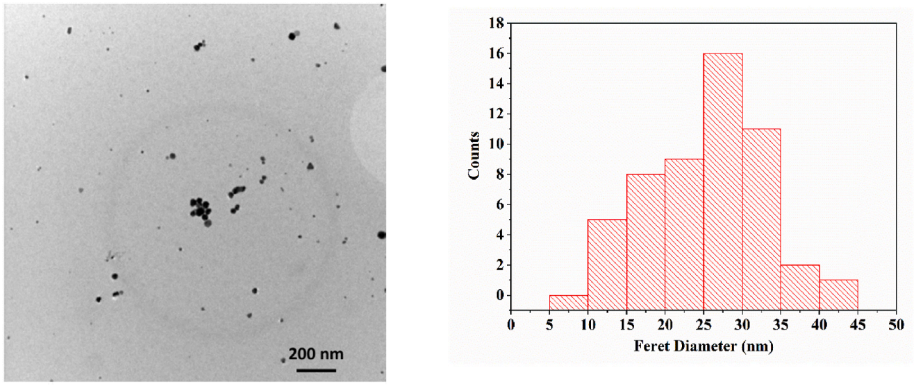

Fig. 1. TEM analysis of Ag NPs. (a) Image illustrating the morphology of spherical silver nanoparticles obtained through laser ablation. (b) Corresponding particle size distribution histogram.

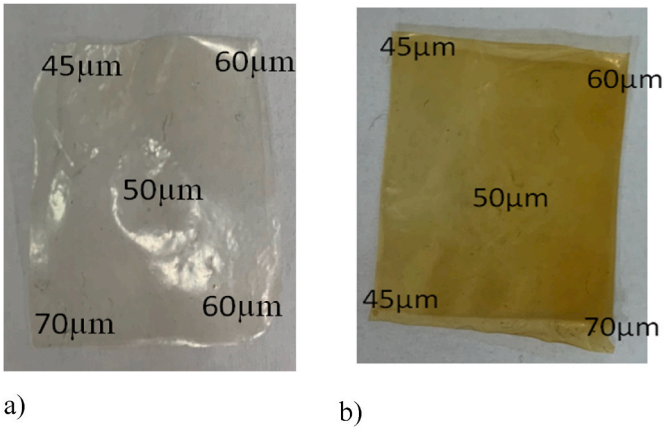

Fig. 2. Optical image of (a) chitosan film and (b) chitosan-silver nanoparticle composite film, both prepared via solvent casting and evaporation. Thickness measurements were conducted in 5 points on both film types and values are shown in the pictures. Film surface dimensions are 25x25mm^2.

using a Fast Fourier Transform, the material transfer complex function $T(\omega)$ was extracted from the ratio of the electric field transmitted through the sample, $E_s(\omega)$ and the reference signal, $E_r(\omega)$. This transfer function correlates with the amplitude and phase changes in the transmitted signal due to refraction and absorption within each sample. The complex index of refraction, $\tilde{n}(\omega) = n(\omega) + ik(\omega)$ extracted from the transfer function was then used to evaluate the complex dielectric function, $\tilde{\varepsilon} = \varepsilon' + \varepsilon''$, where $\varepsilon' = n^2 - k^2$ and $\varepsilon'' = 2nk$

For films, the complex dielectric function was derived from this transfer function using an iterative algorithm that suppresses Fabry–Perot oscillations due to internal reflections within the sample [19–21] by using a commercial analytical software package (TeraLyzer, Menlo Systems). To accurately decouple sample thickness from the refractive index, the algorithm systematically minimizes the artefactual peaks in the quasi-space domain (equivalent to the time-domain echoes) caused by multiple internal reflections within the film.

By shifting the dataset into a quasi-space domain, the true sample thickness at the exact point of THz interrogation is identified at the absolute minimum of the error function. This procedure also enables precise thickness determination with ±1 μm accuracy. To illustrate this minimization process, the normalized quasi-space error peaks are plotted against thickness values in Supplementary Material. Clear global minima are revealed at a localized thickness both for the pure chitosan film and the silver nanoparticle-doped chitosan film spot at arbitrarily chosen points.

Analogous procedure was applied to the Ag NP colloidal suspension and the chitosan solution matrix. For colloidal measurements, a demountable quartz cuvette (Hellma® Type 106-QS, 100 μm path length, purchased via Sigma-Aldrich (Part No. Z805963) was used. The cell windows are made of amorphous synthetic fused silica (Suprasil® quartz) with a nominal wall thickness of 1 mm. In this case, the software also accounts for quartz wall thickness and corresponding Fabry–Perot effects, fixing the colloid thickness at 100 μm.

2.5. Mean field theory and Landau-Looyenga model

To interpret the effective dielectric response of heterogeneous systems with dilute inclusions, the Landau–Looyenga mean field theory was employed.

It is critical to contextualize the selection of this model against other classical effective medium frameworks, such as the Maxwell–Garnett (MG) and Bruggeman (BR) formulations. The Bruggeman model treats both components symmetrically and is ideally suited for high-density composite configurations near or above the electrical percolation threshold. However, as established in our previous work investigating the electron transport properties of silver-doped chitosan [22], which was produced under similar conditions and methods, ensure that the composite is far below percolation limits, rendering the Bruggeman model physically unsuitable [23].

While the Maxwell–Garnett model is conventionally applied to dilute spheres, it exhibits high sensitivity to absolute boundary shapes and breaks down if subtle, non-spherical sub-aggregates form during solvent evaporation [24]. In contrast, the Landau–Looyenga relation operates via a continuous cubic-root dependence on permittivity, which smoothly captures the dominant physics of dilute packing regimes irrespective of minor inclusion shape variances [11].

This model is appropriate for describing the effective permittivity of heterogeneous media with dilute inclusions, like systems where a small volume fraction of guest particles (like Ag NPs) is dispersed within a host medium (the chitosan matrix). It has been successfully applied in various contexts to retrieve dielectric constants of nano powders or colloids including nano-microparticles, provided that the inclusions do not exhibit strong metallic conductivity [25–27].

The Landau-Looyenga equation for the effective dielectric constant of a two-component mixture is typically expressed as:

$$\varepsilon_{eff} = \left[f_1 {\varepsilon_1}^{1/3} + f_2 {\varepsilon_2}^{1/3} \right]^3 \quad (1)$$

where ε_{eff} is the effective dielectric constant of the composite. f_1 and f_2

are the volume fractions ($f_1 + f_2 = 1$), ε_1 and ε_2 are the dielectric constants of component 1 and component 2, respectively.

To solve this relationship uniquely across a scanned surface, the inversion algorithm was strictly constrained by a deterministic parameter-clamping strategy. The host matrix baseline ($\varepsilon_1 = \varepsilon_{Chitosan}$) was locked across all pixels using the dielectric spectrum extracted from pure chitosan control films at 0.5 THz. Simultaneously, the inclusion baseline ($\varepsilon_2 = \varepsilon_{Ag}$) was locked at $\varepsilon_{Ag} \approx -360 + 600i$ based on independent colloidal measurements restricted to a fixed 100 μm liquid layer cell. By treating both constituent dielectric constants as immovable boundaries, the spatial mapping protocol isolates the local volumetric fraction, f_2, as the sole independent free parameter, effectively eliminating mathematical optimization degeneracy.

In this study, the theory allowed for the interpretation of the macroscopic dielectric properties measured by THz-TDS by relating them to the individual dielectric properties and volume fractions of the chitosan matrix and the embedded silver nanoparticles. The volumetric concentration of silver nanoparticles in the colloidal suspension is a crucial parameter for subsequent analysis, enabling the determination of the Ag-NPs' complex dielectric function. The initial Ag NP concentration in the suspension was measured as $7 \cdot 10^{-6}$ gr/cm^3, as detailed in the characterization section 2.1.

Rather than the true bulk density of solid silver (10.49 g/cm^3), for subsequent calculations the density of silver was taken as 0.312 gr/cm^3. This value specifically refers to the apparent density, often called "tapped" or "poured" density. Referring to the previous investigations conducted these silver-doped chitosan films [22], the nanoparticle concentrations utilized in this system sit far below the electrical percolation threshold. Under these highly dilute, non-percolating conditions, the inclusions remain isolated and cannot assemble into a continuous metallic network. Consequently, the local dielectric function extracted for these isolated particles is significantly smaller than bulk solid silver values, as detailed in Section 3.1. Because the particles do not occupy a compact, close-packed solid volume within the fluid-cast polymer matrix for this reason using the true bulk density would be physically incorrect, forcing the effective medium inversion to yield an unphysical permittivity.

The use of this value for silver nanoparticles is well-established in academic literature. This density figure is particularly relevant when these nanomaterials are integrated as fillers in research on composites [28] and is consistently reported as the "bulk" density for commercially procured Ag NPs [29,30]. Based on the assumed density, the volumetric percentage (filling factor) of the NPs can be calculated $\sim 2.2 \cdot 10^{-5}$. This quantified concentration is used as an input for applying effective medium theory and extract the complex dielectric function of the isolated nanoparticles from colloidal measurements, as it will be shown in the next Section.

3. Results and discussion

3.1. Extracting the complex dielectric function of the isolate Ag-NPs

The complex dielectric function $\tilde{\varepsilon} = \varepsilon' + i\varepsilon''$ of the Ag-NPs colloid and of the chitosan solution used as matrix is plotted in Fig. 3(a). The complex dielectric function of the isolated nanoparticles, extracted using the effective mean field theory, is presented in Fig. 3(b).

While the retrieved dielectric function are large, they are fundamentally suppressed by several orders of magnitude relative to the bulk silver values ($\varepsilon' \sim -10^5$) tabulated by Ordal et al. [31]. This significant reduction is physically justified by the finite-size effect in sub-25 nm particles. When the nanoparticle dimensions approach or fall below the bulk electron mean free path, electron-surface scattering becomes the dominant collision mechanism, strongly dampening the collective Drude response, in accordance with the fact that these concentrations lie far below the electrical percolation threshold. The Landau–Looyenga inversion to satisfy the ultra-dilute volume fraction of the isolated inclusions and the extracted permittivity values, accurately reflects this non-percolating regime, and the order-of-magnitude departure from bulk silver baselines confirms that our effective medium approach avoids overestimating the dielectric loading of individual nano-inclusions.

This observation aligns with other THz investigations into similar nanomaterials and is consistent with findings in thin silver films, where both the real and imaginary components of the refractive index decrease with diminishing film thickness [32]. While direct experimental data characterizing the complex dielectric function and the influence of particle size and concentration for Ag colloids are scarce in existing literature, theoretical models, often utilizing Drude or Drude-like approaches, consistently demonstrate a significant deviation from bulk properties. As a reference, we consider the infrared optical constants for bulk silver provided by Ordal et al. [31,33], whose revised Drude parameters serve as a standard benchmark.

3.2. Chitosan film thickness mapping

Terahertz imaging measurements are performed using a raster scan technique in transmission geometry. This involves recording time-domain signals at each spatial location, with a 500 μm step size, over a 120-ps time window. The sample is precisely moved point-by-point using computer-controlled motorized linear stages.

To generate the large-area thickness map, the complex refractive index of dry chitosan at the reference frequency is used as a fixed material parameter. In the present analysis, the value $\tilde{\varepsilon}_{Chitosan} \approx 4.8 + 0.8i$ at 0.5 THz is taken from previously reported data for chitosan films prepared under comparable conditions were characterized after solvent evaporation [22]. The adopted optical constants therefore correspond to the dry solid-state film. This reference refractive index value is then used

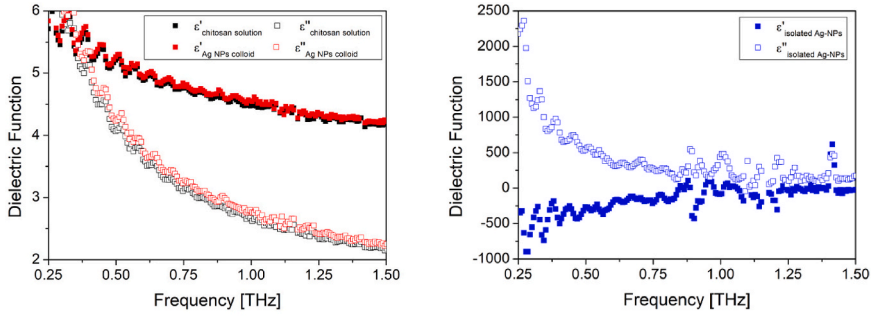

a) b)

Fig. 3. The complex dielectric function derived from THz-TDS for (a) the Ag NPs colloidal suspension and the chitosan solution matrix, and (b) the silver isolated nanoparticles, using their volumetric concentration.

to calculate the local thickness at each pixel across the scanned region.

The detailed characterization of the chitosan film thickness profile is presented in Fig. 4. The resulting thickness maps overall confirm that the central portion of the films exhibits good uniformity, with an average thickness of approximately 50 μm. These results are consistent with the preliminary five-point micrometric measurements (Fig. 2), thereby validating the reproducibility of the casting process.

In Fig. 4(a)–a 3D graph of the large-area (25 × 25 mm^2) thickness map of the chitosan film is shown, revealing a gradual increment from one side of the film to the other, with a mean value of 50 μm in the central portion. This initial overview provides insights into the overall film morphology.

Zooming into a 10 × 10 mm^2 area, Fig. 4(b) displays a 2D contour plot that further elucidates the thickness distribution. Here, the thickness does not follow a simple linear progression but exhibits patterns reminiscent of fluid flow. This non-uniformity is characteristic of films fabricated via solvent casting and evaporation, a method known for challenges in achieving homogeneous distribution due to phenomena such as wetting/dewetting, phase separation, capillary flow, and viscous drag during the process. The non-equilibrium nature of the evaporation process significantly influences the final morphology and can lead to such localized variations in film thickness [17]. This can manifest as density gradients or varied surface roughness depending on the solvent evaporation rate [34]. For instance, a polymer-rich skin layer can form at the liquid/vapor interface, influencing the distribution and accumulation of particles [15].

Fig. 4(c) shows an even smaller area of the sample, 3 × 3 mm^2, corresponding approximately to the THz beam spot size. At this spatial scale, thickness variations are smaller than the ±1 μm uncertainty of the THz thickness retrieval algorithm. This observation is critical for

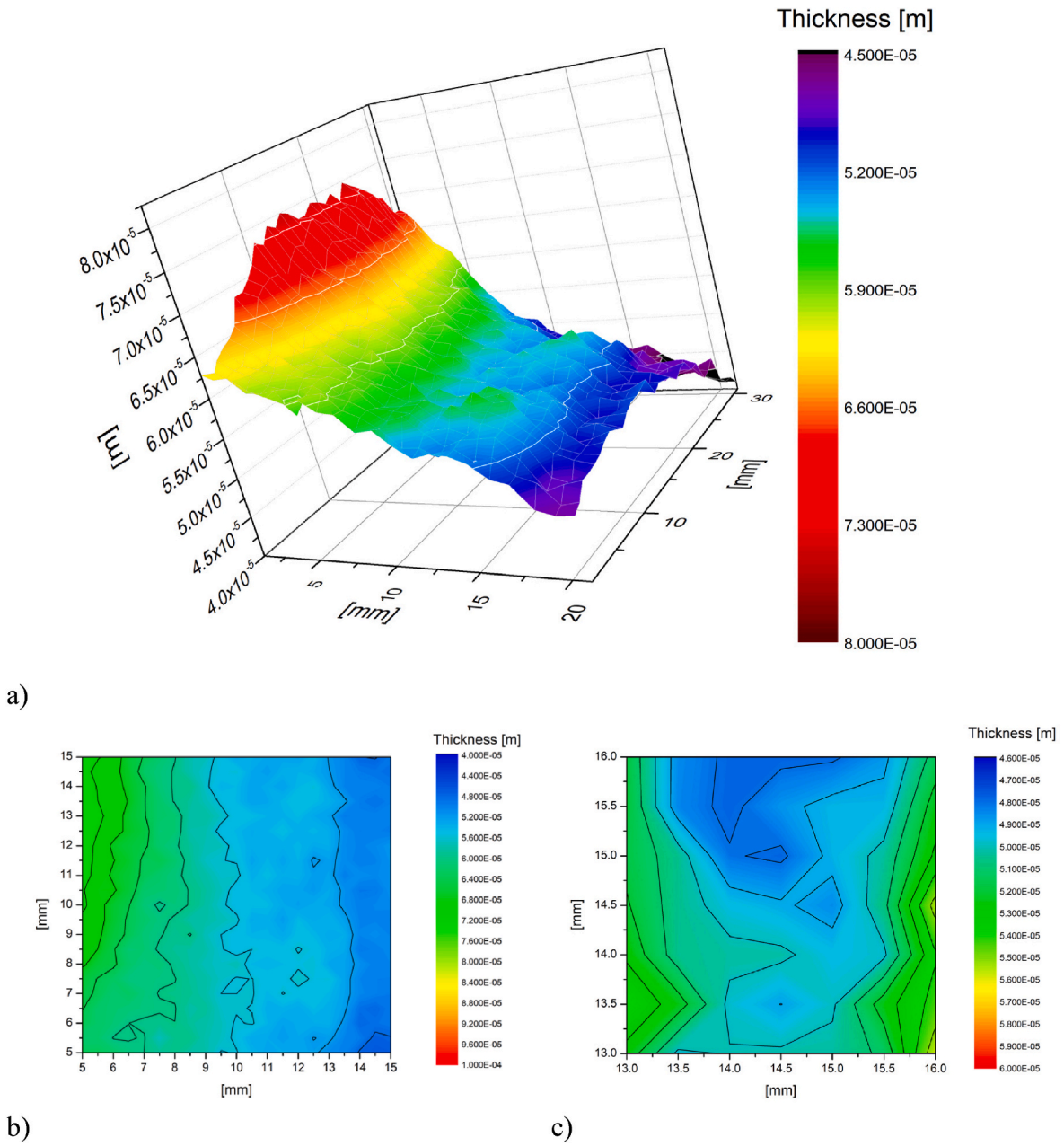

Fig. 4. a) 3D contour plot of the large-area thickness map of the chitosan film, showing a gradual thickness increment and a mean thickness of approximately 50 μm in the central region. b) 2D contour plot of a 10 mm × 10 mm section of the film, revealing non-linear thickness distribution patterns. c) 2D contour plot of a 3 mm × 3 mm section of the film, showing thickness homogeneity at a scale comparable to the THz measurement spot size. 2D maps are displayed using false-colour scale.

subsequent nanoparticle mapping.

Since local thickness variations fall within measurement uncertainty at the interrogation scale, variations in the extracted dielectric response of composite films can be attributed primarily to changes in nanoparticle concentration rather than thickness artifacts.

The thickness mapping therefore establishes a reliable baseline for quantitative interpretation of the nanoparticle fill factor maps presented in the following section.

3.3. Quantification of nanoparticle distribution

THz-TDS imaging is then systematically performed to assess the distribution of silver nanoparticles in the chitosan-Ag NPs composite sample. The primary goal is to precisely determine and map the nanoparticle concentration within the near-center region of the composite film.

This quantitative spatial inversion is performed under the operational assumption that the local film thickness remains fixed at a uniform nominal value of 50 μm within the tightly restricted 4 × 4 mm^2 analysis window. While separate casting suspensions can exhibit divergent fluid-flow patterns across large surface areas due to solvent evaporation dynamics, preliminary multi-point micrometer profiling (Section 2.3) confirms that both film configurations consistently settle into a flat, highly homogeneous thickness plateau within their central core. By confining our effective medium mapping strictly to this pre-verified central plateau and utilizing the rigid error propagation thresholds established in Section 3.2 (where localized thickness deviations of ±1 μm yield a negligible fill-factor uncertainty of only $\delta f_2 \approx \pm 0.0015$), the relative variations in the extracted dielectric response can be reliably translated into spatial gradients of nanoparticle concentration. This localized parameter-clamping approach ensures that the concentration contrast shown in Fig. 5 reflects true relative nanoparticle distribution features rather than unsuppressed casting topography artifacts.

This process involves imaging the composite film point-by-point using THz-TDS to yield the frequency-dependent complex dielectric function at each spatial location across the scanned area. Subsequently, with the known response of the pure chitosan matrix and the individually characterized silver nanoparticles, the Landau-Looyenga mean field theory is applied at each pixel of the THz image to generate the desired maps of nanoparticle distribution. To this aim, dielectric values are specifically selected at 0.5 THz, where the signal-to-noise ratio of the THz signal is at its maximum. The complex dielectric function for the chitosan matrix is taken as $\tilde{\varepsilon}_{Chitosan} \approx 4.8 + 0.8i$, whereas for the isolated Ag-NPs $\tilde{\varepsilon}_{Ag} \approx -360 + 600i$ is used (see Fig. 3(a) and (b), respectively).

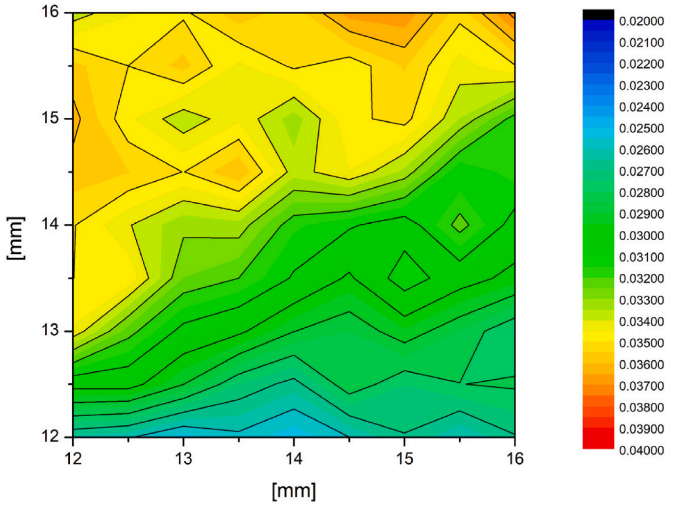

Fig. 5. Spatial map illustrating the local volumetric concentration (fill factor) of silver nanoparticles in a false colour scale within the near-center region of the chitosan-Ag NPs composite film.

By inverting equation (1), the local volumetric concentration of the silver nanoparticles is extracted, enabling the generation of a detailed spatial map illustrating these concentrations across the specified area of the composite film (Fig. 5). The ability to map these critical parameters is invaluable for identifying areas of aggregation or depletion of nanoparticles, directly impacting the material intended properties and guiding improvements in fabrication processes for enhanced homogeneity.

Observing changes in the fill factor map across a 4 × 4 mm^2 area provides valuable evidence for assessing nanoparticle distribution. In this study, a non-destructive diagnostic framework utilizing Terahertz Time-Domain Spectroscopy imaging was developed and implemented to spatially map and quantify these variations.

The scientific validity of these maps relies on understanding their inherent limitations and uncertainties. These include the spatial resolution, limited by the THz wavelength ($\sim 600\mu m$ at 0.5 THz), the 500 μm raster scan step size, and the 1 mm beam spot diameter. Thus, each measured point averages properties over an approximately 1 mm by 1 mm area, smoothing out finer heterogeneity. Film thickness determination also contributes uncertainty; despite the iterative algorithm's precision, a ± 1 μm uncertainty for a 50 μm film introduces a relative error ±2% in the fill factor and particle number. Moreover, the Landau-Looyenga model, while suitable for dilute inclusions, depends on accurate input parameters like the complex dielectric functions of the chitosan matrix and silver nanoparticles. Inaccuracies in these inputs or deviations from model assumptions can introduce systematic biases.

The spatial map shown in Fig. 5 directly depicts the local volumetric concentration of silver nanoparticles. It is generated by inverting the Landau-Looyenga mean field theory, using THz data along with the complex dielectric functions of the chitosan matrix and silver nanoparticles. Although the dielectric function of the Ag NPs—an essential input to this model—exhibits only limited changes due to minor variations in particle dimensions, the numerical values and visual representation of the fill factor on this map remain fixed once generated with these established parameters. However, it is crucial to recognize that the quantification of nanoparticle numbers derived from these fixed fill factor values is highly sensitive to the assumed particle size. This sensitivity arises from the cubic relationship between the fill factor and nanoparticle radius, such that any uncertainty in the assumed mean diameter significantly impacts the calculated values. Therefore, while the fill factor map accurately portrays the volumetric distribution, one should be cautious when using it for exact quantification of the particle count.

To illustrate the correlation between fill factor variations and nanoparticle distribution, we analyzed the mapping of a 50 μm thick film, which revealed a 0.02 variation in the fill factor. This change provides a quantitative measure of how the nanoparticle volume fraction fluctuates across the mapped region. The total interrogated volume at each scanning position is defined by the beam spot dimension and the retrieved film thickness, resulting in an estimated volume of $2 \times 10^{-10}\ m^3$. Then, knowing the approximate volume of a single 25 nm diameter spherical Ag NP ($V_{NP} = 4.16 \times 10^{-24}\ m^3$), the number of particles corresponding to each fill factor can be determined by dividing the total volume occupied by nanoparticles. At a fill factor of 0.02, the number particles $N_{0.02}$ in this area contains approximately 4.89 10^{11} particles. When the fill factor increases to 0.04, the number of particles $N_{0.04}$ rises to about 9.78 10^{11}. Therefore, an absolute change of 0.02 in the fill factor corresponds to a substantial change of approximately $\Delta N = N_{0.04} - N_{0.02} \approx 4.89 \times 10^{11}$ particles within that area. This demonstrates that even seemingly small numerical differences in the fill factor represent significant variations in the local nanoparticle count, directly reflecting changes in particle distribution.

To evaluate the statistical significance of the extracted nanoparticle

gradients against sub-micron topographical variations, a rigorous error propagation analysis was conducted (see Section S2 of the Supplementary Information). Given an algorithmic thickness uncertainty of ±1 μm on a nominal 50 μm film, the maximum baseline error propagated to the extracted effective permittivity is $\Delta\varepsilon_{eff} \approx \pm 0.105$. When inverted through the Landau–Looyenga relation, the extreme magnitude of the isolated nanoparticle dielectric response acts as a mathematical dampener in the denominator. This heavily suppresses the propagation error, yielding a strict absolute fill factor uncertainty of only $\Delta f_2 \approx \pm 0.002$ (a relative fluctuation of ±2%).

When these perturbed effective permittivity bounds (ε_{min} *and* ε_{max}) are inverted back through the effective medium model, the resulting artefactual fill factor calculation deviates by an absolute maximum of only $\delta f_2 \approx \pm 0.0015$, yielding an artificial baseline window between 0.0185 and 0.0215. Conversely, the actual spatial variations recorded in the experimental concentration map (Fig. 5) span a much wider range from 0.020 to 0.040, establishing a true physical contrast gradient of $\Delta f_2 = 0.020$. Since the observed spatial features exceed the maximum possible thickness-induced error margin by more than a factor of ten, the quantitative variations across the mapped central region are definitively verified to track genuine nanoparticle concentration fluctuations rather than artefactual topography noise.

While direct, destructive spatial elemental mapping (such as ICP-MS or micro-XRF) was not conducted, the quantitative reliability of the retrieved volumetric concentrations is robustly supported by macroscopic formulations and microstructural parameters. The initial film composition was fixed during solution preparation at a controlled loading of 0.8 wt% silver nanoparticles. Microstructural analysis via TEM confirmed a highly uniform, non-aggregated morphology with a narrow size distribution cantered at a mean diameter of 25 nm, validating our treatment of the fillers as discrete, isolated inclusions within the dilute host matrix. Furthermore, the spatial integrity of the fill factor maps was internally cross-checked against the localized error limits of our THz thickness-retrieval algorithm. Because local thickness variations at the interrogation scale remain negligible, the observed spatial gradients are proven to track true compositional dispersion rather than topographical artifacts.

Overall, these results show that THz-TDS imaging can be used not only as a qualitative contrast mechanism, but also as a quantitative tool for assessing nanoparticle dispersion in thin polymeric films. The preliminary thickness mapping of the pure chitosan film provides an essential reference, showing that, at the spatial scale probed by the THz beam, local thickness variations are sufficiently small to be distinguished from dielectric variations associated with the embedded nanoparticles. At the same time, the independent extraction of the dielectric response of the Ag NPs allows the effective medium model to be locally inverted, converting the measured THz dielectric contrast into a spatially resolved volumetric fill factor. While the absolute particle-number estimate remains sensitive to assumptions on particle diameter, spatial averaging, film thickness, and the parameters of the Landau–Looyenga model, the method reliably identifies relative variations in nanoparticle concentration over the investigated area. This capability is particularly relevant for solvent-cast nanocomposite films, where evaporation-driven flow, aggregation, and local depletion can produce spatial inhomogeneities that are difficult to access non-destructively.

THz-TDS imaging therefore emerges as a practical diagnostic method for evaluating filler dispersion and correlating local dielectric contrast with the spatial distribution of components within advanced nanocomposites, thereby supporting their optimized design, processing, and application.

4. Conclusion

This study presents a non-destructive methodology for mapping nanoparticle distribution in thin-film composites by integrating Terahertz Time-Domain Spectroscopy imaging with effective medium modelling.

The TDS analysis of both the silver nanoparticle colloidal suspension and the chitosan solution matrix; this allows for the characterization of the isolated nanoparticles' unique dielectric properties via mean-field theory, accounting for deviations from bulk silver behaviour at terahertz frequencies. Following this, the chitosan and the composite thin films were characterized independently. Morphological and spectroscopic analysis of the chitosan film established a necessary baseline, revealing a uniform mean thickness of approximately 50 μm in the central regions. In contrast, larger-area mapping captured fluid-flow patterns characteristic of solvent-casting evaporation dynamics. By quantifying these topographical variations, the study ensures that subsequent dielectric fluctuations extracted from the composite film maps are definitively attributed to local nanoparticle concentration rather than physical thickness artifacts. Ultimately, the dielectric properties of the isolated nanoparticles, the chitosan film, and the composite film were integrated to invert the Landau–Looyenga effective medium relation at each spatial pixel. This inversion enabled the calculation of local volumetric fill factors and the generation of detailed nanoparticle distribution maps. Error propagation analysis further confirmed the quantitative validity of the framework against topographical artifacts. A worst-case thickness uncertainty of ±1 μm propagates to an absolute fill factor error of only $\Delta f_2 \approx \pm 0.002$. This high precision is achieved because the massive dielectric response of the isolated metallic inclusions mathematically dampens sensitivity during effective medium inversion. This proves that the extracted spatial variations are statistically significant and definitively track true nanoparticle concentration gradients rather than local film roughness. While spatial resolution remains constrained by the terahertz wavelength and beam spot size, this approach provides a robust, area-resolved measurement of filler dispersion, offering a practical framework for evaluating the internal structure and homogeneity of solvent-cast functional nanocomposites. These outcomes can also be applied to investigate alternative deposition techniques like spin coating, helping to clarify how varying processing methodologies dictate the final sub-micron uniformity and internal filler distribution.

CRediT authorship contribution statement

Can Koral: Writing – review & editing, Writing – original draft, Visualization, Validation, Software, Methodology, Investigation, Formal analysis, Data curation, Conceptualization. **Michela Marsico:** Writing – review & editing, Visualization, Validation, Formal analysis. **Angela De Bonis:** Writing – review & editing, Visualization, Validation, Resources. **Zahra Mazaheri:** Writing – review & editing, Validation. **Gian Paolo Papari:** Writing – review & editing, Visualization, Validation. **Antonello Andreone:** Writing – review & editing, Visualization, Validation, Resources.

Declaration of generative AI and AI-assisted technologies in the writing process

During the preparation of this work the author(s) used [Jenni.Ai] in order to improve language and readability. After using this tool/service, the author(s) reviewed and edited the content as needed and take(s) full responsibility for the content of the publication.

Funding sources

This research was partially supported by the Istituto Nazionale di Fisica Nucleare (INFN), Project “ATHENAE".

Declaration of competing interests

The authors declare that they have no known competing financial interests or personal relationships that could have appeared to influence

the work reported in this paper.

Appendix A. Supplementary data

Supplementary data to this article can be found online at https://doi.org/10.1016/j.matchemphys.2026.133024.

Abbreviations

THz	Terahertz
TDS	Time Domain Spectroscopy
NPs	Nanoparticles

Data availability

Data will be made available on request.

References

[1] P. Petrik, M. Fried, Mapping and imaging of thin films on large surfaces, Phys. Status Solidi Appl. Mater. Sci. 219 (13) (2022), https://doi.org/10.1002/pssa.202100800.

[2] I. Issahaku, I.K. Tetteh, A.Y. Tetteh, Chitosan and chitosan derivatives: recent advancements in production and applications in environmental remediation, Environ. Adv. (2023), https://doi.org/10.1016/j.envadv.2023.100351.

[3] H.S. Oh, K.T. Nam, Invited paper: application of chitin and Chitosan toward electrochemical hybrid device, Electron. Mater. Lett. (2011), https://doi.org/10.1007/s13391-011-0302-9.

[4] K. Kulka, A. Sionkowska, Chitosan based materials in cosmetic applications: a review, Molecules (2023), https://doi.org/10.3390/molecules28041817.

[5] I. Aranaz, et al., Chitosan: an overview of its properties and applications, Polymers (2021), https://doi.org/10.3390/polym13193256.

[6] E. Prokhorov, J.G. Luna-Bárcenas, J.B. González-Campos, I.C. Sanchez, Conductivity mechanisms in a composite of chitosan-silver nanoparticles, Mol. Cryst. Liq. Cryst. (2011), https://doi.org/10.1080/15421406.2011.538327.

[7] J. Hernández-Vargas, et al., Chitosan/MWCNTs-decorated with silver nanoparticle composites: dielectric and antibacterial characterization, J. Appl. Polym. Sci. (2014), https://doi.org/10.1002/app.40214.

[8] H. Hoshina, et al., Polymer morphological change induced by terahertz irradiation, Sci. Rep. (2016), https://doi.org/10.1038/srep27180.

[9] R.A. Ilyas, et al., Natural-Fiber-reinforced chitosan, chitosan blends and their nanocomposites for various advanced applications, Polymers (2022), https://doi.org/10.3390/polym14050874.

[10] M. Borovkova, M. Khodzitsky, P. Demchenko, O. Cherkasova, A. Popov, I. Meglinski, Terahertz time-domain spectroscopy for non-invasive assessment of water content in biological samples, Biomed. Opt. Express (2018), https://doi.org/10.1364/boe.9.002266.

[11] L.D. Landau, E.M. Lifshitz, A.L. King, Electrodynamics of continuous media, Am. J. Phys. (1961), https://doi.org/10.1119/1.1937882.

[12] C. Koral, B. Ortaç, H. Altan, A case study: the negative THz time shift observed for Cu nanoparticle colloids, Next Res. 2 (4) (2025) 100973, https://doi.org/10.1016/j.nexres.2025.100973.

[13] C. Koral, B. Ortaç, H. Altan, Terahertz time-domain study of silver nanoparticles synthesized by laser ablation in organic liquid, IEEE Trans. Terahertz Sci. Technol. 6 (4) (2016) 525–531, https://doi.org/10.1109/TTHZ.2016.2572360.

[14] R. Casini, G. Papari, A. Andreone, D. Marrazzo, A. Patti, P. Russo, Dispersion of carbon nanotubes in melt compounded polypropylene based composites investigated by THz spectroscopy, Opt. Express 23 (14) (2015) 18181, https://doi.org/10.1364/oe.23.018181.

[15] S. Cheng, G.S. Grest, Dispersing nanoparticles in a polymer film via solvent evaporation, ACS Macro Lett. 5 (6) (2016) 694–698, https://doi.org/10.1021/acsmacrolett.6b00263.

[16] G. Amarandei, C. O'Dwyer, A. Arshak, U. Thiele, U. Steiner, D. Corcoran, Effect of Au nanoparticle spatial distribution on the stability of thin polymer films, Langmuir 29 (22) (2013) 6706–6714, https://doi.org/10.1021/la400659q.

[17] J.U. Kim, B. O'Shaughnessy, Morphology selection of nanoparticle dispersions by polymer media, Phys. Rev. Lett. 89 (23) (2002) 2–5, https://doi.org/10.1103/PhysRevLett.89.238301.

[18] M. Marsico, et al., Alternative source of chitosan for the direct laser synthesis of Ag@chitosan composites with antibacterial and photocatalytic properties, Next Mater. 9 (July) (2025), https://doi.org/10.1016/j.nxmate.2025.100952.

[19] M. Scheller, C. Jansen, M. Koch, Analyzing sub-100-μm samples with transmission terahertz time domain spectroscopy, Opt. Commun. (2009), https://doi.org/10.1016/j.optcom.2008.12.061.

[20] I. Pupeza, R. Wilk, M. Koch, Highly accurate optical material parameter determination with THz time-domain spectroscopy, Opt. Express (2007), https://doi.org/10.1364/oe.15.004335.

[21] T.D. Dorney, R.G. Baraniuk, D.M. Mittleman, Material parameter estimation with terahertz time-domain spectroscopy, J. Opt. Soc. Am. A (2001), https://doi.org/10.1364/JOSAA.18.001562.

[22] C. Koral, et al., Enhanced relaxation dynamics in silver-doped chitosan nanocomposites : probing the charge carrier dynamics and terahertz dielectric response, Mater. Chem. Phys. 344 (March) (2025) 131137, https://doi.org/10.1016/j.matchemphys.2025.131137.

[23] G. Bánhegyi, Numerical analysis of complex dielectric mixture formulae, Colloid Polym. Sci. (1988), https://doi.org/10.1007/BF01451527.

[24] V. Markel, Introduction to the Maxwell Garnett Approximation : Tutorial Vadim Markel to Cite This Version : HAL Id : Hal-01282105 Introduction to Maxwell Garnett Approximation : Tutorial, 2016.

[25] G. Papari, C. Koral, T. Hallam, G.S. Duesberg, A. Andreone, Terahertz spectroscopy of amorphous WSe2and MoSe2thin films, Materials 11 (9) (2018), https://doi.org/10.3390/ma11091613.

[26] C. Imparato, et al., RSC advances photocatalytic hydrogen evolution by co-catalyst-, RSC Adv. 10 (2020) 12519–12534, https://doi.org/10.1039/D0RA01322F.

[27] C. Koral, et al., Defects in the amorphous−crystalline evolution of gel-derived TiO2, J. Phys. Chem. C (2020), https://doi.org/10.1021/acs.jpcc.0c07568.

[28] R.S. Negi, R.S. Bisht, R.K. Singh, Physico-mechanical and antibacterial properties of pine gum/epoxy composites with/without silver nanoparticles, Macromol. Mater. Eng. 304 (7) (2019) 1–12, https://doi.org/10.1002/mame.201800744.

[29] R.K. Sahoo, Preparation of polypropylene/silver nanoparticles nanocomposite films and evaluation of its barrier and antimicrobial properties for packaging applications, Int. J. Res. Appl. Sci. Eng. Technol. 9 (VIII) (2021) 764–774, https://doi.org/10.22214/ijraset.2021.37430.

[30] R.K. Sahoo, B.P. Panda, S.K. Nayak, S. Mohanty, Mechanical and morphological investigation of virgin polyethylene and silver nanoparticle-loaded nanocomposites film: comprehensive analysis of kinetic models for non-isothermal crystallization, Bull. Mater. Sci. 40 (2) (2017) 307–320, https://doi.org/10.1007/s12034-017-1370-8.

[31] M.A. Ordal, R.J. Bell, R.W. Alexander, L.L. Long, M.R. Querry, Optical properties of fourteen metals in the infrared and far infrared: Al, Co, Cu, Au, Fe, Pb, Mo, Ni, Pd, Pt, Ag, Ti, V, and W, Appl. Opt. (1985), https://doi.org/10.1364/ao.24.004493.

[32] H.T. Lee, et al., Measuring complex refractive indices of a nanometer-thick superconducting film using terahertz time-domain spectroscopy with a 10 femtoseconds pulse laser, Crystals 11 (6) (2021), https://doi.org/10.3390/cryst11060651.

[33] M.A. Ordal, L.L. Long, R.J. Bell, S.E. Bell, R.R. Bell, R.W. Alexander Jr., C. A. WardOptical properties of the metals Al 22 (1983) 1099–1120. https://doi.org/10.1364/AO.22.001099. Pd, Pt, Ag, Ti, and W Co, Cu, Au, Fe, Pb, Ni.

[34] S. Sakthinathan, et al., A Review of Thin-Film Growth , Properties , Applications , and Future Prospects, 2025.